nature communications

Article

https://doi.org/10.1038/s41467-024-54984-7

A one-step fabrication of soft-magnetic high entropy alloy fiber with excellent strength and flexibility

Received: 22 June 2024

Accepted: 26 November 2024

Published online: 04 December 2024

Check for updates

Yan Ma[1,2,7], Zongde Kou[3,7], Weiming Yang[1] ✉, Aina He[2], Yaqiang Dong[2], Qikui Man[2], Haishun Liu[4], Zhiming Li[5], Akihisa Inoue[6] & Jiawei Li[2] ✉

Soft-magnetic fibers (SMFs) play a crucial role in energy conversion, transmission, and storage within electronic devices. However, conventional SMFs have poor plasticity and are therefore difficult to withstand long-term tensile, torsional, and shear deformation. A high fraction of grain boundaries could improve plastic deformability of conventional SMFs, but deteriorates the coercivity. This severely limits their applications in flexible electronics and multifunctional components. Herein, we propose a strategy to overcome this dilemma, which is realized by coarsening the grains of a $Fe_{34}Co_{29}Ni_{29}Al_3Ta_3Si_2$ high entropy alloy (HEA) fiber containing ordered coherent nanoprecipitates with small lattice misfit via a simple one-step in-rotating-water spinning method. This allows to reduce domain wall pinning and improve dislocation mobility. The resultant micron-diameter soft-magnetic HEA fiber has a tensile strength of 674 MPa at 23% elongation, a low coercivity of 8.1 Oe, a moderate magnetization of 116 emu/g at 10 kOe and a high Curie temperature of 770 K.

Soft-magnetic fibers (SMFs) with low coercivity (H_c), such as Co-based and Fe-based amorphous and polycrystalline fibers, are fundamental materials that serve in sensors, actuators, and electromagnetic shielding devices, etc.[1–7]. Recently, permalloys and Co/Fe-based SMFs have obtained significant attention owing to their potential applications in geomagnetic navigation, human-computer interaction, and human-like tactile sensing. However, due to limited stretchability, the large-scale production and application of SMFs and related devices still face numerous challenges[8]. With the advancement of flexible electronics and multifunctional components, there is a substantial need for micrometer-scale SMFs capable of enduring tensile, torsional, and shear loads in long-term operations[9,10]. These fibers necessitate not only just exceptional soft magnetic performance but also miniaturization, great tensile strength and plasticity. Traditional approaches for achieving a low H_c usually involve annealing to release internal stress and trigger nanocrystallization in amorphous SMFs, which can induce brittleness[11–13]. Enhancing the mechanical strength of SMFs by precipitation usually compromises plasticity and H_c[14,15]. Therefore, it is challenging to achieve a good balance among these seemingly contradictory requirements.

Since the first introduction of high entropy alloys (HEAs) in 2004[16,17], HEAs have become an innovative design concept that is promising to overcome the tradeoff between strength and plasticity[18–22]. In addition to extensive research on their mechanical properties, there has been a growing interest in the soft magnetic properties of HEAs[23–25]. For instance, the bulk FeCoNiTaAl HEA with nanoscale coherent precipitates exhibits a tensile strength of 1336 MPa at 54% tensile elongation, a low H_c of 0.98 Oe, and a moderate

[1]School of Mechanics and Civil Engineering, State Key Laboratory for Geomechanics and Deep Underground Engineering, China University of Mining and Technology, Xuzhou, China. [2]CAS Key Laboratory of Magnetic Materials and Devices, Zhejiang Province Key Laboratory of Magnetic Materials and Application Technology, Ningbo Institute of Materials Technology and Engineering, Chinese Academy of Sciences, Ningbo, Zhejiang, China. [3]Herbert Gleiter Institute of Nanoscience, School of Material Science and Engineering, Nanjing University of Science and Technology, Nanjin, China. [4]School of Materials and Physics, China University of Mining and Technology, Xuzhou, China. [5]School of Materials Science and Engineering, Central South University, Changsha, China. [6]International Institute of Green Materials, Josai International University, Togane, Japan. [7]These authors contributed equally: Yan Ma, Zongde Kou.
✉e-mail: wmyang@cumt.edu.cn; lijw@nimte.ac.cn

saturation magnetization (M_s) of 1.10 T[11,12]. The dual-phase $Fe_{26}Co_{25}Ni_{20}Cu_{15}Al_{13.1}Ga_{0.9}$ HEA with coherent nanoprecipitates have a balance of compressive strength (1448 MPa), compressive strain (200 %), and H_c (4.19 Oe)[13]. The single-phase $(Co_{30}Fe_{45}Ni_{25})_{0.8}(Al_{40}Si_{60})_{0.2}$ HEA has a combination of high compressive strength of 1636 MPa, relatively high M_s of 1.24 T, and low H_c of 0.75 Oe[26]. It has been recognized that HEAs with high structural disorder, designable crystal structure, and variable magnetic properties can balance plasticity and H_c by tuning particle/matrix interfacial coherency stresses to maximize the interaction strength with dislocations and minimize the pinning of magnetic domain walls[11]. However, current research on soft magnetic HEAs is mainly limited to bulk, thin films, and powders[13,23,27–29]. The soft magnetic and mechanical properties of micron-diameter fibers have been rarely investigated in the field of HEAs, although several recent reports illustrated the mechanical properties of millimeter-sized HEA fibers prepared by the hot drawing method[14,30,31]. It has been recognized that traditional casting and thermomechanical processing techniques are not suitable for obtaining micro-diameter HEA fibers[30,31]. It is still challenging to achieve micro-diameter HEA fibers through one-step simple preparation methods, particularly when optimized mechanical and soft-magnetic properties are required.

For crystalline soft magnetic alloys ($FeSi_{6.5}$, $Fe_{50}Ni_{50}$, etc), when the grain size is between 1 μm and 1 mm, the H_c decreases with grain coarsening, satisfying the relationship as $H_c \propto 1/D$ (D is the grain size)[32]. Also, coarse-grained structure is usually beneficial to plasticity[33]. In this work, an in-rotating-water spinning method is first used to achieve micron-diameter SMFs with coarse-grained structures through a short, energy-saving, and high-efficiency process[34,35]. The metalloid element Si is introduced into the Fe-Co-Ni-Al-Ta system to suppress the pinning effects of Ta and effectively improve the plasticity without deteriorating H_c[36,37]. Accordingly, SMFs with nominal compositions $Fe_{34}Co_{29}Ni_{29}Al_3Ta_3Si_2$ and a diameter of ~180 μm are fabricated by the one-step in-rotating-water spinning method. The HEA fibers have a good balance of H_c and tensile elongation, outperforming the other SMFs. This work thus ensures the compatibility of mechanical and soft magnetic properties of SMFs under multi-dimensional deformations and high temperatures, facilitating their large-scale production and application in emerging fields such as wearable electronics, humanoid robots, and intelligent construction.

Results and Discussion

Magnetic and mechanical properties of HEA fibers

Figure 1a shows the schematic diagram of the in-rotating-water spinning method[38]. The continuous fibers prepared by this method could reach hundreds of meters in length and achieve a diameter of ~180 μm, with uniform axial dimensions and smooth surface (Fig. 1b). The as-spun fibers, as shown in Fig. 1c, can be bent into a complexly curvy shape, such as a superplastic spring which can also be easily attracted by a magnet and extended to several times its original length, demonstrating an excellent combination of mechanical flexibility and soft magnetism. The fibers were annealed to further tailor the mechanical and magnetic performance. The magnetic hysteresis loops of HEA fibers before and after annealing are shown in Fig. 1d. As the annealing time increases, there is no significant change in magnetization (~116 emu/g at 10 kOe). The H_c of HEA fibers significantly decrease from 8.1 Oe in the as-spun sample to 2.7 Oe in the 800 °C-120 min annealed sample, and then slowly decrease to 1.1 Oe in the 300 min-annealed sample (Supplementary Fig. S2). The Curie temperature of the as-spun and 800 °C-120 min annealed samples are 770 and 690 K, respectively (Supplementary Fig. S3), indicating the excellent high-temperature tolerance of the alloys. Figure 1e presents the tensile stress-strain curves of the HEA fibers at different states. The ultimate tensile strength (σ_u) and fracture elongation (ε_f) of the as-spun sample are 674 MPa and 23.4 %, respectively. The 800 °C-10 min annealed sample shows a good combination of tensile strength (σ_u = 835 MPa) and fracture elongation (ε_f = 9.9%). The σ_u for the 800 °C-120 min annealed sample reaches 1029 MPa at a cost of the plasticity of ~20 %. The yield strength increased significantly with increased annealing temperature, while plasticity deteriorated obviously (Supplementary Fig. S4). The tensile fracture elongation and H_c of the HEA fibers and other typical SMFs are summarized in Fig. 1f. The tensile elongation of the HEA fibers in our work outperforms all other SMFs, and the H_c of the HEA fibers is lower than that of FeCo, FeSi, and metal deposited

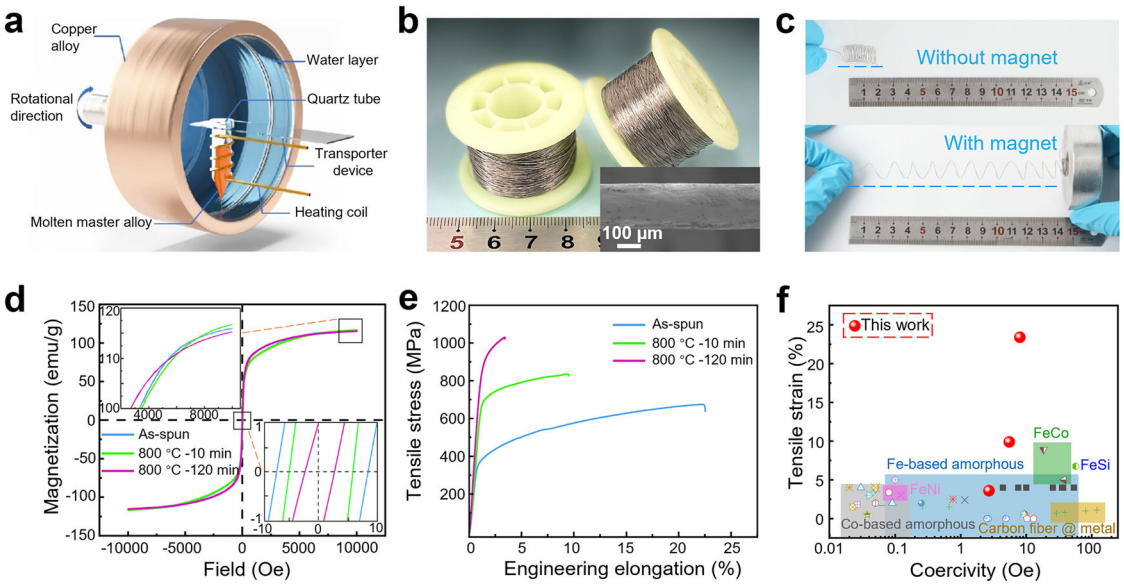

Fig. 1 | Manufacturing, morphology, and properties of the present soft magnetic high entropy alloy (HEA) fibers. a Schematic diagram of the in-rotating-water spinning method. **b** Image of the wound HEA fibers. Insert (bottom right) is the scanning electron microscope (SEM) image of a HEA fiber. **c** Images of spring-shaped HEA fibers with and without magnet. **d** Magnetic hysteresis loops and **e** tensile engineering stress-strain curves of HEA fibers. The inset in **d** shows the enlarged view of the trend of changes in saturation magnetization and coercivity. **f** Tensile elongation and coercivity of the present HEA fibers compared to those of other soft-magnetic fibers (SMFs)[5,10,39–49]. Source data for Fig. 1d and e are provided as a Source data file.

https://doi.org/10.1038/s41467-024-54984-7

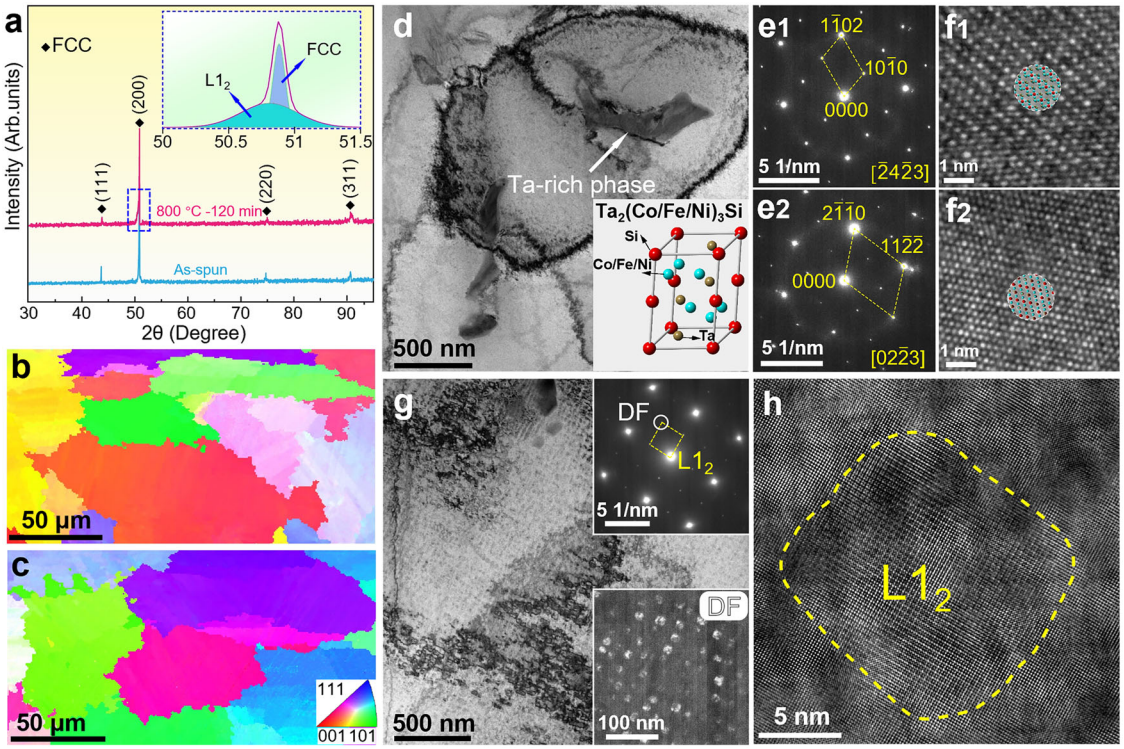

Fig. 2 | Microstructural evolution of HEA fibers. a X-ray diffraction (XRD) pattern of HEA fibers (Insert is the deconvolution of the diffraction peak of the HEA fibers). Electron backscatter diffraction (EBSD) inverse pole figure (IPF) images of **b** as-spun and **c** 800 °C-120 min annealed HEA fibers. **d** Bright field transmission electron microscope (BF-TEM) image of as-spun HEA fibers, showing a Ta-rich phase in the face-centered cubic (FCC) matrix. Insert is the crystal structure of $Ta_2(Co/Fe/Ni)_3Si$. The red atom, brown atom and blue atom represent Si, Ta, and Fe/Co/Ni elements respectively. Selected area electron diffraction (SAED) images were taken along **e1** [$\bar{2}4\bar{2}3$] and **e2** [$02\bar{2}3$] zone axes of the Ta-rich phase. Corresponding high-resolution transmission electron microscope (HRTEM) images of **e** and overlapping projections of the $Ta_2(Co/Fe/Ni)_3Si$ lattice along **f1** [$\bar{2}4\bar{2}3$] and **f2** [$02\bar{2}3$] zone axes. The Ta-rich phase was identified to be $Ta_2(Co/Fe/Ni)_3Si$ according to the SAED patterns, as illustrated **d** in the inset of **d**. **g** BF-TEM image of 800 °C-120 min annealed HEA fibers. The upper and lower insets of **g** are the corresponding SAED and dark field transmission electron microscope (DF-TEM) images, respectively. **h** HRTEM image showing a $L1_2$ nanoprecipitate. Source data for Fig. 2a are provided as a Source data file.

carbon fibers etc. (see Supplementary Tab. S1 for detailed information)[5,10,39–49].

Microstructure analysis

Microstructure characterization was performed by using multiple methods to reveal the microstructural evolution of the HEA fibers upon annealing. The XRD results (Fig. 2a) of as-spun fibers shows a face-centered cubic (FCC) structure. The small peak ($2\theta = 50.8°$) detected in the 800 °C-120 min annealed HEA fibers besides the FCC (200) peak corresponds to the $L1_2$ structure. By the deconvolution of diffraction peaks, the lattice constant of the $L1_2$ precipitates and the FCC matrix are determined to be 0.3109 nm and 0.3105 nm, respectively, corresponding to a lattice misfit of ~0.14%. Electron backscatter diffraction (EBSD) inverse pole figure (IPF) images (Fig. 2b, c) detect no obvious difference between the as-spun and annealed HEA fibers: both samples show a nearly equiaxed morphology of grains. The average grain sizes estimated from the IPF images are approximately 48 μm and 57 μm for the as-spun and 800 °C-120 min annealed fibers, respectively, with the grains elongated slightly along the longitudinal direction due to the manufacturing process of the fibers. The transmission electron microscopy (TEM) characterizations were further carried out to study the microstructure of the as-spun (Fig. 2d–f) and 800 °C-120 min annealed HEA fibers (Fig. 2g, h). Figure 2d shows the bright-field (BF) TEM image of the as-spun fibers, in which Ta-rich phase with an average size of approximately 310 nm was observed (Supplementary Fig. S5a). According to the elemental composition (Fig. S5) and selected area electron diffraction (SAED) patterns along different zone axes (Fig. 2e1, 2), the Ta-rich phase was identified to be $Ta_2(Co/Fe/Ni)_3Si$ (space group No.: 194, $a = 4.8$ Å, $c = 7.6$ Å), as illustrated in the inset of Fig. 2d. Fig. 2f1 and f2 are high-resolution TEM (HRTEM) images of the Ta-rich phase taken along [$\bar{2}4\bar{2}3$] and [$02\bar{2}3$] zone axes, respectively, coinciding well with the $Ta_2(Co/Fe/Ni)_3Si$ phase, as confirmed by the overlapping projections of the $Ta_2(Co/Fe/Ni)_3Si$ lattice. After annealed at 800 °C for 120 min, the $L1_2$ precipitates with an average size of 18 ± 2 nm were detected as indicated by the SAED and dark-field (DF) TEM images inserted in Fig. 2g. Compared with the as-spun state (Fig. 2d), the content of Ta-rich phase is obviously reduced or even disappeared. The HRTEM image in Fig. 2h confirms the ordered $L1_2$ phase (outlined by the dotted yellow line) which shows full coherency with matrix lattice. The $L1_2$ phase has a near-spherical structure, which is related to the interfacial free energy of the particles[50]. It is mainly composed of Ta, Al, and Ni elements (Supplementary Fig. S5b).

Figure 3a–c display the three-dimensional atom probe tomography (3D APT) results of FCC matrix of the as-spun fibers. It shows uniform elemental distribution within a sub-nanometer scale (Supplementary Fig. S6). Figure 3d visualizes the near-spherical $L1_2$ nanoprecipitates in terms of a 3D reconstruction of a typical APT tip for the 800 °C-120 min annealed sample. Figure 3e provides a cross-sectional two-dimensional (2D) concentration plot in terms of a 30 at. % Ni threshold value, acquired from the center region of the APT tip (Fig. 3d). From Fig. 3e, we selected two representative precipitate/matrix interfaces for further characterization (red dashed square). These results evidence Ni enrichment in the precipitates and Fe enrichment in the matrix, respectively. Figure 3f shows 1D compositional profiles acquired across a selected precipitate (see red arrow in

https://doi.org/10.1038/s41467-024-54984-7

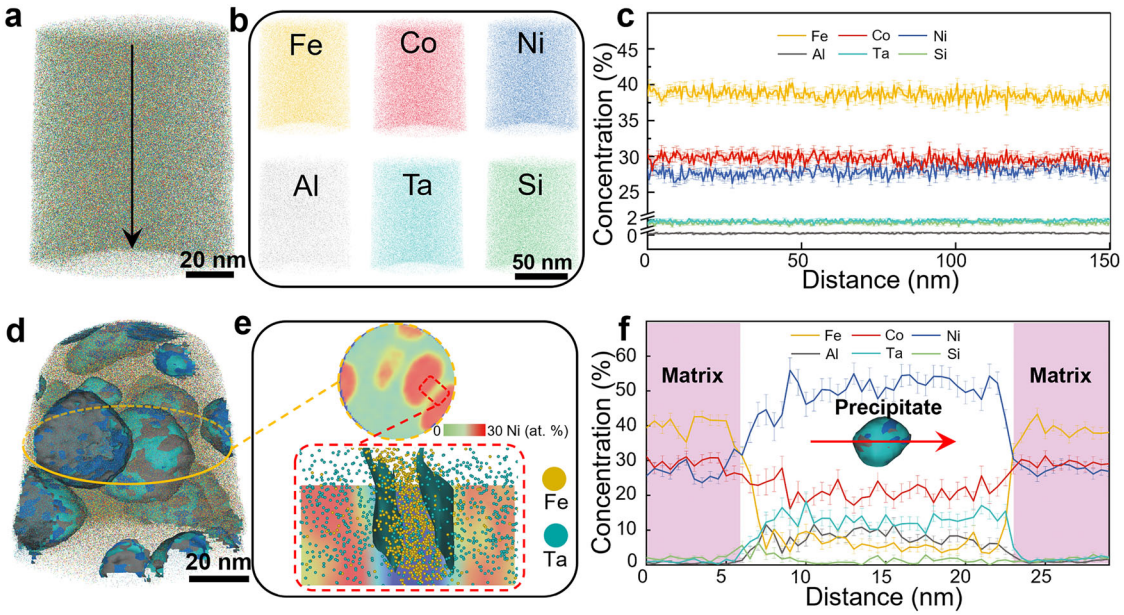

Fig. 3 | Three-dimensional atom probe tomography (3D-APT) maps of HEA fibers. a 3D-APT map of as-spun HEA fibers. **b** The uniform distribution of all elements in near atomic-scale in **a**. **c** 1D compositional profiles across the tip with the direction marked by the dark arrow in **a**. **d** 3D-APT map of 800 °C-120 min annealed HEA fibers. **e** 2D projection of the Ni concentration slice acquired from the central part of the APT tip shown in **d** and enlarged view of the groove region showing the distribution of Fe and Ta atoms. **f** 1D compositional profiles showing the compositional changes across a selected precipitate along the red arrow shown in the inset. Error bars in **c** and **f** refer to the standard deviations of one experiment. The size of the error is related to the number of atoms within a single data point. Source data for Fig. 3c and f are provided as a Source data file.

the inset of Fig. 3f). The chemical compositions of the FCC and the $L1_2$ phases were derived and averaged from several APT sub-volumes (Fig. S7). The 3D-APT results are well consistent with the high-angle annular dark field scanning transmission electron microscopy observations (Supplementary Fig. S5b). Introducing nanoscale $L1_2$ phases has recently been proven to be an effective precipitation strengthening method in FCC HEAs[51–53]. The profiles in Fig. 3f reveals the enrichment of Ni (50.2 at.%), Al (11.6 at.%) and Ta (11.2 at.%), whose concentrations are much higher than those in the master alloy (29 at.% Ni, 3 at.% Al, and 3 at.% Ta). Al can act as a strong $L1_2$ former in Ni/Co containing HEAs[54], while the addition of Ta promotes the continuous precipitation of $L1_2$ particles[55]. Since the ordered $L1_2$ precipitates are much stronger than the FCC solid solution matrix, higher stresses are thus required for dislocations in matrix to cut through the $L1_2$ precipitates, which leads to a significant improvement of strength (Fig. 1e). These nanosized hard particles dispersed in matrix also degenerate the dislocation storage ability by reducing the mean free path of dislocations, thus giving rise to the decreased plasticity (Fig. 1e).

Mechanisms of magnetization

The magnetization and H_c are the key parameters of soft magnetic materials[56]. The vacancies in 3 *d* atomic orbitals of Fe, Co and Ni atoms contribute to the magnetic moments, and these vacancies will be filled up by the outer shell electrons of Al and Si elements[57]. The samples exhibit a stable magnetization at 10 kOe (Supplementary Fig. S2) owing to the magnetic exchange interaction from certain atomic ratio. Upon different annealing conditions, the Ta-rich phase occupies only a small fraction (1.2%), thus having a negligible effect on magnetization. To gain further insights into the low H_c mechanism of HEA fibers, their magnetic domain structures were observed by Lorentz-TEM (LTEM) (Fig. 4a, b). For the as-spun fibers (Fig. 4a), as the magnetic field increases from 0 Oe to 333 Oe, domain walls 4 and 5 disappears, whereas domain walls 1, 2, and 3 remain pinned at the boundary of the Ta-rich phase even when the magnetic field increase to 1000 Oe. The domain wall motion is still dominant during the magnetization process, resulting in a small H_c of 8.1 Oe. The magnetic domain walls of LTEM samples were indicated (Supplementary Fig. S8). The dynamic process of the domain wall motion was recorded (Supplementary Movies 2, 3). The domain wall thickness δ_w can be estimated by ref. 58

$$\delta_w = \pi(A_{ex}/K_1)^{1/2} \quad (1)$$

where $A_{ex} = k_B T_c/2a_0$ is the exchange stiffness, $k_B = 1.38 \times 10^{-23}$ J K^{-1} is the Boltzmann's constant, and T_c and a_0 are the Curie temperature and lattice parameter of the FCC matrix respectively (see Supplementary Table S2). K_1 is the first magnetocrystalline anisotropy constant (10.4 KJ m^{-3})[11]. The domain wall thickness of the as-spun and annealing HEA fibers is therefore estimated to be 119 nm and 112 nm, respectively. The pinning of the domain wall motion is caused by the Ta-rich phase (Supplementary Fig. S9). Its size in the FCC matrix reaches approximately 310 nm, which is larger than the domain wall width. Thus, the $Ta_2(Co/Fe/Ni)_3Si$ particles with size exceeding the critical domain wall width will form and pin the domain wall movement[59] (arrow 1 in Fig. 4a). However, the volume fraction of the particles in the as-spun HEA fibers is only 1.2%, thus having limited effect on increasing the H_c.

For the 800 °C-120 min annealed fibers, weak pinning effects can be observed. As the magnetic field increases, domain walls 1, 2, and 3 move smoothly and disappear when the magnetic field reaches 1000 Oe (Fig. 4b). Compared with the as-spun fibers, a lower external magnetic field is required to reach saturation state in the 800 °C-120 min annealed fibers with a smaller H_c of 2.7 Oe. After long-duration annealing (60 - 300 min), the size and volume fraction of the Ta-rich phase further decrease. Meanwhile, a uniformly distributed coherent $L1_2$ precipitates with a size of ~18 nm. Due to the grain size of the HEA fibers is above the critical single-domain size, the H_c decreases with grain coarsening, following

https://doi.org/10.1038/s41467-024-54984-7

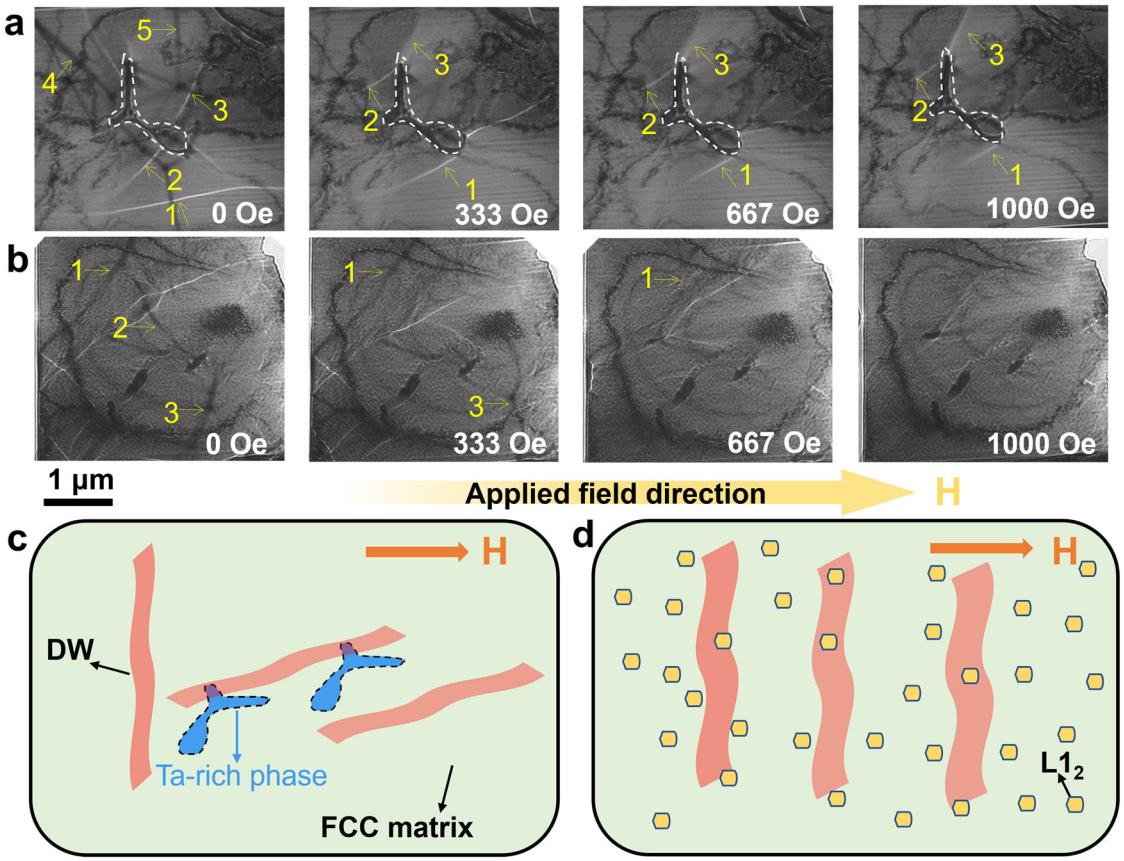

Fig. 4 | Magnetic domain structure and low H_c mechanism of HEA fibers. Lorentz transmission electron microscopy (LTEM) images taken from as-spun **a** and 800 °C-120 min annealed **b** HEA fibers. The yellow arrows labeled 1, 2, 3, 4, and 5 in **a** and **b** represent the magnetic domain walls (DWs). **c** Schematic diagram showing the pinning effect of precipitates on domain walls of as-spun HEA fibers. **d** Schematic diagram showing the smooth movement of domain walls of 800 °C–120 min annealed HEA fibers.

the model for the grain size dependence of the H_c as ref. 13

$$H_C \approx \frac{p(K_1 + \frac{3}{2}\lambda_S\sigma)\beta^{1/3}\delta_W}{\mu_0 M_S^2 D} \quad (2)$$

where p, K_1, λ_s, σ, β, δ_w, and D represent the coefficient, the magnetocrystalline anisotropy constant, the magnetostriction constant, the internal residual stress, the impurity concentration, the domain wall thickness, and the grain size, respectively. According to the model, the magnitude of the decrease in H_c owing to grain coarsening is negligible compared with the experimentally observed values. In addition, the H_c gradually decreases with annealing time (Supplementary Fig. S2), resulting in the decrease in β and σ for the annealed fibers. On the one hand, the size of $L1_2$ nanoprecipitates in the annealed fibers is less than 20 nm (Fig. 2), which is far smaller than the domain wall width. On the other hand, the multiple coherent interfaces of FCC/$L1_2$, can greatly diminish the internal strain in the fibers, and weaken the domain wall pinning by precipitates and phase boundary[13]. Therefore, the domain walls in FCC phase can be easily pulled out from these $L1_2$ nanoprecipitates, resulting in the low H_c, as demonstrated in Fig. 4b.

Based on the above discussion, the interactions of the Ta-rich phase and $L1_2$ precipitates with magnetic domains are schematically illustrated in Fig. 4c and d, respectively. The slightly larger H_c of the as-spun fibers compared to previously reported $(Co_{30}Fe_{45}Ni_{25})_{1-x}(Al_{40}Si_{60})_x$ bulk HEAs is due to the pinning effect of the Ta-rich phase on the movement of the domain wall and the influence of localized stress[26]. The 800 °C-120 min annealed fibers have a lower H_c owing to the cooperative effect of stress relaxation, the disappearance of Ta-rich phase, and the formation of $L1_2$ coherent nanocrystals.

Deformation mechanism

Figure 5a and b are the SEM images of fracture surfaces of the as-spun and 800 °C-120 min annealed HEA fibers taken along radial and axial directions of fibers, in which the as-spun fibers show a better plastic deformability than the annealed fibers. Meanwhile, the as-spun fibers have a rougher fracture surface with deeper and larger dimples than that of the annealed fibers which also indicates a superior plasticity of the as-spun fibers over the annealed ones. The fracture surface is composed of the central region of brittle fracture and the surface region of plastic fracture caused by surface constraint effect[60,61]. EBSD-IPF images and their corresponding KAM maps showing the local misorientation were also obtained at the deformed region near the tensile fracture, as displayed in Fig. 5a and b. It is seen that the grains in the as-spun fibers are elongated along the tensile direction while those in the 800 °C-120 min annealed fibers remain nearly equiaxed (see EBSD-IPF images in Fig. 5a and b). KAM maps reflecting the density of geometrically necessary dislocations in Fig. 5a and b show that the dislocations in the as-spun fibers are much more than in 800 °C-120 min annealed fibers[62], indicating that the dislocation activities are more pronounced in the as-spun fibers. In addition, the distribution of dislocations in the as-spun fibers is also comparatively wide (>200 μm from the fracture) and more homogeneous than that in the 800 °C-120 min annealed fibers in which dislocations distribute mainly adjacent to the fracture region and grain boundaries (GBs). In-situ tensile test results in SEM-EBSD mode confirm the result (see Supplementary

https://doi.org/10.1038/s41467-024-54984-7

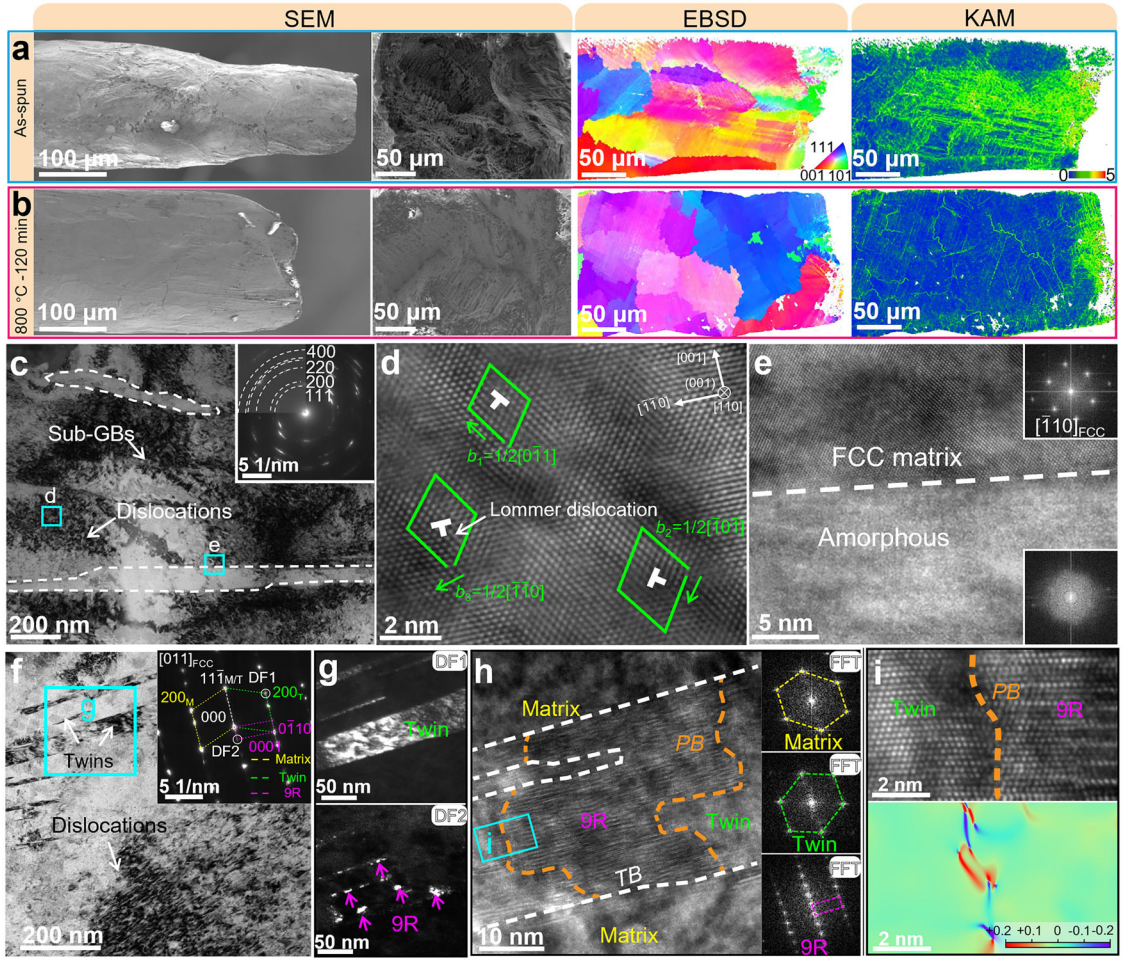

Fig. 5 | Deformation structure of the present soft magnetic HEA fibers. Substructure evolution observed after tensile tests for the as-spun **a** and 800 °C −120 min annealed **b** HEA fibers: SEM images showing the difference of fracture surface; IPF and kernel average misorientation (KAM) maps showing the distributions of deformation-induced misorientations; **c** BF TEM image showing the microstructure of deformed region of the as-spun HEA fibers, with the deformation induced amorphous phase outlined by dotted white lines. Inset is the corresponding SAED patterns. **d** HRTEM image of the framed region d in c, showing the dislocations and their interaction. **e** HRTEM image of the framed region e, showing the deformation-induced amorphous in the matrix. **f** BF TEM image showing the microstructure of the deformed region of the 800 °C-120 min annealed HEA fibers. Inset is the corresponding SAED patterns, in which the deformation twin and 9 R phase can be identified. **g** DF TEM images of the framed region in **g**, obtained by using the $(020)_{twin}$ and $(0001)_{9R}$ reflections, respectively. **h** HRTEM image showing the deformation twin and 9 R phase in the matrix, along with the fast Fourier transform (FFT) images of each structure. **i** Enlarged HRTEM image and its corresponding geometric phase analysis (GPA) stress map of the framed region in **h**, showing the interface between the twinned crystal and 9 R phase.

Fig. S10 and 11 and Supplementary Movie 1). These phenomena indicate that dislocation nucleation, multiplication, and motion are more readily activated in the as-spun fibers, therefore possessing a larger plasticity.

In order to understand the deformation mechanism of the HEA fibers in detail, TEM characterization was conducted (Fig. 5c–i). Figure 5c shows the microstructure of the deformed region of the as-spun fibers, where massive dislocations and the resultant sub grain boundary (sub-GBs) can be observed. The SAED patterns inset shows clearly grain refinement. Region d in Fig. 5c was further studied at the HRTEM mode, as displayed in Fig. 5d where two glissile dislocations with the Burgers vectors (BVs) of $\mathbf{b}_1 = 1/2[0\bar{1}1]$ and $\mathbf{b}_2 = 1/2[\bar{1}0\bar{1}]$ and a Lommer dislocation with the BV of $\mathbf{b}_3 = 1/2[\bar{1}\bar{1}0]$ were identified. Given that $\mathbf{b}_1 + \mathbf{b}_2 = \mathbf{b}_3$, the formation of Lommer dislocation indicates the interactions between glissile dislocations. In addition to dislocations, some martensite-like plates appear in the matrix as indicated by dotted white lines in Fig. 5c. Region e in Fig. 5c was amplified at HRTEM mode as displayed in Fig. 5e. It was found that the martensite-like phase is amorphous, as revealed by the FFT insets in Fig. 5e. Deformation induced amorphization generally occurs as a complementary/alternative deformation mechanism in scenarios where dislocation activities are suppressed or insufficient to accommodate the imposed strain[63–66,67,68]. As a specific deformation mechanism, amorphization itself can contribute to plasticity by introducing plastic strain which stems from the volume change and shear band development[69]. Moreover, compared to its crystalline counterpart, amorphous structure is at a higher energy state where extra energy is required during the crystal-to-amorphous transformation. The consumption of extra energy shall inhibit the initiation of micro-cracks by alleviating stress concentration at the intersections of dislocations and thus contribute to ductility[70]. Deformation-induced amorphization has also been reported in other HEAs like FCC-structured FeCoCrNi[71], CrMnFeCoNi[63,65,70], and $Al_{0.1}$CoCrFeNi[72], which is originated from significant accumulations and severe interactions of dislocations, twins and stacking faults. A recent study on BCC-structured TiHfZrNb system HEAs has revealed that amorphization can even take place in an elastic regime due to a large elastic strain (~10%)[73]. The observation in Fig. 5a was conducted on a TEM sample lifted out from the region near the fracture of the fiber using a FIB machine, where severe plastic deformation occurs as testified by KAM maps in Fig. 5a and abundant

dislocations in Fig. 5c. Therefore, the amorphization in the as-spun HEA fibers should be due to dislocation accumulations near the fracture. Regarding the $Ta_2(Co/Fe/Ni)_3Si$ particles, our observations show that they act as dislocation accumulation and nanovoid nucleation sites during deformation (see Supplementary Fig. S12). Since the volume fraction of the $Ta_2(Co/Fe/Ni)_3Si$ particles in the as-spun HEA fibers is only 1.2%, their contribution to the mechanical properties is negligible.

Figure 5f shows the deformed microstructure of the 800 °C-120 min annealed fibers. The SAED patterns (inset of Fig. 5f) reveal that the deformation twin and a 9 R structure are introduced in the FCC matrix. Displayed in Fig. 5g are the DF TEM images of region g framed in Fig. 5f obtained by using the $(020)_{twin}$ and $(0001)_{9R}$ reflections, which shows clearly the twin lamella and 9 R particles indicated by arrows. A detailed HRTEM morphology of the deformation structure was given in Fig. 5h where the twin boundaries (TBs) between matrix and twin crystals and the phase boundaries (PBs) between FCC and 9 R phases are indicated by dotted lines. FFT images of the matrix, twin, and 9 R phase in Fig. 5h are well consistent with the SAED patterns. It was interesting to notice that the 9 R phases have a size comparable to the $L1_2$ phases and seem to form only inside the twin crystals (Fig. 5h and i), which may be attributed to the interaction between Shockley partial dislocations (i.e., twinning dislocations) and the $L1_2$ phases. The increase in strength is mainly attributed to the precipitation-strengthening effect provided by the high-volume fraction of $L1_2$ particles. Region i in Fig. 5h is enlarged in Fig. 5i, along with its geometric phase analysis (GPA) strain map provided below the HRTEM image. It was observed in the GPA map that the PB is effective in blocking dislocations and thus contributes to strengthening.

In conclusion, micron-scale SMFs with excellent strength and flexibility have been successfully achieved via Si microalloying and one-step in-rotating-water spinning method in the Fe-Co-Ni-Al-Ta HEA. Coarsening the grains of a $Fe_{34}Co_{29}Ni_{29}Al_3Ta_3Si_2$ HEA fiber containing ordered coherent nanoprecipitates with small lattice misfit can breed abundant dislocation proximity, resulting in high strength. In addition, the domain wall pinning smaller than the width of the domain wall in the coarse grains is the main reason for the lower H_c. The strength, plasticity, and H_c of the SMFs can be further tailored by annealing. This work provides a technology for the preparation of large plastic SMFs, breaking through the bottleneck of insufficient plasticity of SMFs for decades, and has important significance for promoting the application of HEAs in the field of flexible electronics and multifunctional composites.

Methods

Materials preparation

The ingots with the nominal atomic composition of $Fe_{34}Co_{29}Ni_{29}Al_3Ta_3Si_2$ were prepared by arc melting a mixture of pure metals and pure metalloids (purity ≥ 99.8 wt.%) in an argon atmosphere. HEA fibers with a diameter of approximately 180 μm were prepared using the in-rotating-water spinning method[38]. The copper roller with a diameter of 500 mm is rotating with the speed of 280 r/min during the process. A deionized water layer with a thickness of 20 mm was formed under centrifugal force inside the rotating copper roller. The master alloy in a quartz tube was melted to 1550 °C. A jet of the molten alloy was ejected by argon at a pressure of 0.45 MPa through an orifice of the quartz tube into the rotating water layer. The jet of molten alloy was rapidly cooled into solid fibers, with a cooling rate ranging between 10^4 and 10^6 °C/s[74]. The distance between the orifice and the water layer was 4 mm and the incident angle of the jet to the water layer was 60 °. The fibers were annealed for 10 min, 60 min, 120 min, 180 min, and 300 min at 800 °C under a vacuum degree of 5×10^{-3} Pa, followed by water quenching.

Magnetic and mechanical properties tests

The Hysteresis loops (*M-H* curves) were obtained by a Physical Properties Measurement System (PPMS-Evercool, Quantum Design) equipped with a standard vibrating sample magnetometry (VSM) option in an external magnetic field of ± 10000 Oe at a magnetic field-sweeping rate of 50 Oe/s. Each sample for VSM consists of four 3 mm long fibers interlaced at a 45° angle to eliminate demagnetization and magnetic anisotropy. To obtain accurate H_c, the rate between -100 Oe and 100 Oe was 2 Oe/s.

Tensile tests of the fibers were conducted by a universal testing machine (Zwick/Roell Z1.0) at a strain rate of 5×10^{-3} /s under ambient conditions (~25 °C). The test samples were prepared according to the ASTM D3379-75 standard, as shown in Supplementary Fig. S1[75]. The gauge length of the specimens was 10 mm. The key to sample preparation is to prevent fiber slippage during loading. Two ends of the fibers were fixed on the cardboard using super strong adhesive (AWG97027). In order to mitigate the effect of handling on the samples, a protective layer of cardboard was utilized. The parts connecting the two sides were cut away after gripping the test machine. Only the results in which the fibers failed approximately at the middle of the gauge length were adopted[60]. At least five tests were performed to eliminate experimental errors.

The in-situ tensile SEM-EBSD testing system was produced by QiYue technology. The SEM version used is TESCAN S8000, equipped with an EBSD detector (BrukerE-flash 1000). The samples were elongated at a rate of 1 μm/s by a micro-tensile testing machine.

Microstructure characterization

The phase composition of the fibers was determined by X-ray diffraction (XRD, Burkle D8 Discover) with Cu-Kα radiation. The diffraction peaks were identified based on FCC and $L1_2$ type structure by standard JCPDS (Card No. 65-5131 and 65-0140) data, respectively. The fracture surfaces of fibers were investigated via a scanning electron microscope (SEM, Carl Zeiss Auriga) operated at 5 kV. The morphological analysis of the grains within the samples was conducted through electron backscatter diffraction (EBSD), facilitated on an SEM (Verios G4 UC, Thermo Fisher Scientific). The transmission-electron-microscopy (TEM) samples were prepared by using a focused ion beam (FIB, Carl Zeiss Auriga) facility, and observed in a transmission electron microscope (TEM, Talos F200X, Thermo Fisher Scientific) equipped with a Lorenz lens at 200 kV. In-situ dynamic observation of magnetic viscosity was performed using Lorentz transmission electron microscopy (LTEM) and a self-made horizontal magnetic in-situ sample holder. In focus distance, over focus distance, and under focus distance are −1.29 mm, −380 μm, and −2.21 mm, respectively. The Fresnel mode with a defocus of ~920 μm was used for observation. Three-dimensional atom probe tomography (3D APT) experiments were performed in a Cameca Instruments LEAP 4000X HR in either voltage or laser (pulse energy: 60 pJ, λ = 365 nm, 200 kHz pulse repetition rate) modes, the specimen was kept at a temperature of 50 K. The detection rate was kept at a frequency of 1 ion in every 100 pulses.

Data availability

All data needed to evaluate the conclusions are presented in the paper and the Supplementary Materials. Source data are provided with this paper.

References

1. Charles, A., Rider, A., Brown, S. & Wang, C. Multifunctional magneto-polymer matrix composites for electromagnetic interference suppression, sensors and actuators. *Prog. Mater. Sci.* **115**, 100705 (2021).
2. Feng, T. et al. Real-time self-monitoring and smart bend recognizing of fiber-reinforced polymer composites enabled by embedded magnetic fibers. *Compos. Sci. Technol.* **232**, 109869 (2023).

3. Qin, F. & Peng, H. Ferromagnetic microwires enabled multifunctional composite materials. *Prog. Mater. Sci.* **58**, 183–259 (2013).
4. Pei, C. et al. Superlattice-shelled nanocrystalline core structural design for highly sensitive GMI sensors. *Acta Mater.* **255**, 119088 (2023).
5. Chiriac, H. & Óvári, T. Amorphous glass-covered magnetic wires: preparation, properties, applications. *Prog. Mater. Sci.* **40**, 333–407 (1996).
6. Jurc R., et al. 28 - Sensoric application of glass-coated magnetic microwires. In: *Magnetic Nano- and Microwires (Second Edition)* (ed Vázquez M). Woodhead Publishing (2020).
7. Zhukov A, Ipatov M, Corte-Leon P, Blanco J, Zhukova V. Advanced magnetic microwires for sensing applications. In: *Encyclopedia of Materials: Electronics* (ed Haseeb ASMA). Academic Press (2023).
8. Yang, H. et al. Advances in flexible magnetosensitive materials and devices for wearable electronics. *Adv. Mater.* **2311996**, 1–33 (2024).
9. Xiao, H. et al. Dual mode strain–temperature sensor with high stimuli discriminability and resolution for smart wearables. *Adv. Funct. Mater.* **33**, 2214907 (2023).
10. Zhang, Y. et al. Enhanced magnetoimpedance effect of carbon fiber/Fe-based alloy coaxial composite by tensile stress. *Carbon* **93**, 451–457 (2015).
11. Han, L. et al. A mechanically strong and ductile soft magnet with extremely low coercivity. *Nature* **608**, 310–316 (2022).
12. Han, L. et al. Ultrastrong and ductile soft magnetic high-entropy alloys via coherent ordered nanoprecipitates. *Adv. Mater.* **33**, 2102139 (2021).
13. Li, Z. et al. Strength, plasticity and coercivity tradeoff in soft magnetic high-entropy alloys by multiple coherent interfaces. *Acta Mater.* **254**, 118970 (2023).
14. Chen, J. et al. Ultra-strong heavy-drawn eutectic high entropy alloy wire. *Acta Mater.* **243**, 118515 (2022).
15. Jiang, S. et al. Surface microstructural design to improve mechanical and giant magneto-impedance properties of melt-extracted CoFe-based amorphous wires. *Mater. Des.* **204**, 109642 (2021).
16. Yeh, J. et al. Nanostructured high-entropy alloys with multiple principal elements: novel alloy design concepts and outcomes. *Adv. Eng. Mater.* **6**, 299–303 (2004).
17. Cantor, B., Chang, I., Knight, P. & Vincent, A. Microstructural development in equiatomic multicomponent alloys. *Mater. Sci. Eng. A* **375-377**, 213–218 (2004).
18. Liu, D. et al. Exceptional fracture toughness of CrCoNi-based medium and high-entropy alloys at 20 kelvin. *Science* **378**, 978–983 (2022).
19. Gludovatz, B. et al. A fracture-resistant high-entropy alloy for cryogenic applications. *Science* **345**, 1153–1158 (2014).
20. Zhang, C. et al. Strong and ductile FeNiCoAl-based high-entropy alloys for cryogenic to elevated temperature multifunctional applications. *Acta Mater.* **242**, 118449 (2022).
21. Gou, S. et al. Additive manufacturing of ductile refractory high-entropy alloys via phase engineering. *Acta Mater.* **248**, 118781 (2023).
22. Jo, Y. et al. Cryogenic strength improvement by utilizing room-temperature deformation twinning in a partially recrystallized VCrMnFeCoNi high-entropy alloy. *Nat. Commun.* **8**, 15719 (2017).
23. Chaudhary, V., Chaudhary, R., Banerjee, R. & Ramanujan, R. Accelerated and conventional development of magnetic high entropy alloys. *Mater. Today* **49**, 231–252 (2021).
24. Zhang, J. et al. Native oxidation and complex magnetic anisotropy-dominated soft magnetic CoCrFeNi-based high-entropy alloy thin films. *Adv. Sci.* **9**, 2203139 (2022).
25. Orbay, Y. et al. Magnetic properties of the FCC and BCC phases of $(MnFeCoNi)_{80}Cu_{20-x}Z_x$ (Z: Al, Ga) high-entropy alloys. *Acta Mater.* **259**, 119240 (2023).
26. Zhou, K. et al. FeCoNiAlSi high entropy alloys with exceptional fundamental and application-oriented magnetism. *Intermetallics* **122**, 106801 (2020).
27. Gao, W. et al. Novel CoFeAlMn high-entropy alloys with excellent soft magnetic properties and high thermal stability. *J. Mater. Sci. Technol.* **153**, 22–31 (2023).
28. Gao, W. et al. Effects of structural transformation on magnetic properties of AlCoFeCr high-entropy soft magnetic powder cores by adjusting Co/Fe ratio. *Mater. Des.* **225**, 111537 (2023).
29. Yan, J. et al. Anomalous size effect on yield strength enabled by compositional heterogeneity in high-entropy alloy nanoparticles. *Nat. Commun.* **13**, 2789 (2022).
30. Li, D. et al. High-entropy $Al_{0.3}$CoCrFeNi alloy fibers with high tensile strength and ductility at ambient and cryogenic temperatures. *Acta Mater.* **123**, 285–294 (2017).
31. Li, D., Gao, M., Hawk, J. & Zhang, Y. Annealing effect for the $Al_{0.3}$CoCrFeNi high-entropy alloy fibers. *J. Alloy. Compd.* **778**, 23–29 (2019).
32. Herzer, G. Modern soft magnets: amorphous and nanocrystalline materials. *Acta Mater.* **61**, 718–734 (2013).
33. Jia, Y. et al. Efficient coarse-grained superplasticity of a gigapascal lightweight refractory medium entropy alloy. *Adv. Sci.* **2207535**, 1–12 (2023).
34. Ochin, P. et al. Shape memory thin round wires produced by the in rotating water melt-spinning technique. *Acta Mater.* **54**, 1877–1885 (2006).
35. Inoue, A., Hagiwara, M. & Masumoto, T. Production of Fe-P-C amorphous wires by in-rotating-water spinning method and mechanical-properties of the wires. *J. Mater. Sci.* **17**, 580–588 (1982).
36. Wei, D. et al. Si-addition contributes to overcoming the strength-ductility trade-off in high-entropy alloys. *Int. J. Plast.* **159**, 103443 (2022).
37. Zhang, Y., Zuo, T., Cheng, Y. & Liaw, P. High-entropy alloys with high saturation magnetization, electrical resistivity and malleability. *Sci. Rep.* **3**, 1455 (2013).
38. Masumoto, T., Ohnaka, I., Inoue, A. & Hagiwara, M. Production of Pd-Cu-Si amorphous wires by melt spinning method using rotating water. *Scr. Met.* **15**, 293–296 (1981).
39. Kefu, Y. et al. Research progress and application prospect of Fe-based soft magnetic amorphous/nanocrystalline alloys. *Acta Phys. Sin.* **67**, 016101 (2018).
40. Han, Y. et al. Syntheses and fundamental properties of Fe-rich metastable phase alloys with saturation magnetization exceeding 1.9 T. *Mat. Res.* **100**, 367–370 (2015).
41. Zhang, J. et al. Thin and flexible Fe-Si-B/Ni-Cu-P metallic glass multilayer composites for efficient electromagnetic interference shielding. *ACS Appl. Mater. Inter.* **9**, 42192–42199 (2017).
42. Shi, M., Liu, Z. & Zhang, T. Effects of metalloid B addition on the glass formation, magnetic and mechanical properties of FePCB bulk metallic glasses. *J. Mater. Sci. Technol.* **31**, 493–497 (2015).
43. Shi, Z., Li, R., Li, X., Wang, C. & Zhang, T. Controllable brittleness in soft-magnetic Fe-P-C-B metallic glasses through composition design. *Mater. Sci. Eng. A* **766**, 138385 (2019).
44. Ma, Z. et al. Ultrathin, flexible, and high-strength Ni/Cu/metallic glass/Cu/Ni composite with alternate magneto-electric structures for electromagnetic shielding. *J. Mater. Sci. Technol.* **81**, 43–50 (2021).
45. Bruno, N. et al. The effect of stress-annealing on the mechanical and magnetic properties of several Fe-based metal-amorphous nano-

composite soft magnetic alloys. *J. Non-Cryst. Solids* **600**, 122037 (2023).
46. Yazdanmehr, M., Anijdan, S. & Bahrami, A. Using GA-ANN algorithm to optimize soft magnetic properties of nanocrystalline mechanically alloyed Fe-Si powders. *Comp. Mater. Sci.* **44**, 1218–1221 (2009).
47. Yamazaki, T., Katabira, K., Narita, F., Furuya, Y. & Nakao, W. Microstructure-enhanced inverse magnetostrictive effect in Fe-Co alloy wires. *Adv. Eng. Mater.* **22**, 2000026 (2020).
48. Zhukov, A. et al. Magnetostriction of Co-Fe-based amorphous soft magnetic microwires. *J. Electron. Mater.* **45**, 226–234 (2016).
49. Shuai, S., Lu, S., Xiang, Z. & Lu, W. Stress-induced giant magneto-impedance effect of amorphous CoFeNiSiPB ribbon with magnetic field annealing. *J. Magn. Magn. Mater.* **551**, 169131 (2022).
50. Ardell, A. & Nicholso, R. On modulated structure of aged Ni-Al alloys. *Acta Met.* **14**, 1295–1309 (1966).
51. Yang, T. et al. Multicomponent intermetallic nanoparticles and superb mechanical behaviors of complex alloys. *Science* **362**, 933–937 (2018).
52. He, J. et al. A precipitation-hardened high-entropy alloy with outstanding tensile properties. *Acta Mater.* **102**, 187–196 (2016).
53. Fan, L. et al. Ultrahigh strength and ductility in newly developed materials with coherent nanolamellar architectures. *Nat. Commun.* **11**, 6240 (2020).
54. Zhao, Y. et al. Development of high-strength Co-free high-entropy alloys hardened by nanosized precipitates. *Scr. Mater.* **148**, 51–55 (2018).
55. Qi, W. et al. Effects of Ta microalloying on the microstructure and mechanical properties of $L1_2$-strengthened CoCrFeNi-AlTi high-entropy alloys. *Mater. Sci. Eng. A* **875**, 145048 (2023).
56. Michael et al. Amorphous and nanocrystalline materials for applications as soft magnets. *Prog. Mater. Sci.* **40**, 333–407 (1999).
57. Mitera, M., Naka, M., Masumoto, T., Kazama, N. & Watanabe, K. Effects of metalloids on the magnetic properties of iron based amorphous alloys. *Phys. Status Solidi A* **49**, K163–K166 (1978).
58. Bitoh, T., Makino, A. & Inoue, A. Origin of low coercivity of Fe-(Al, Ga)-(P, C, B, Si, Ge) bulk glassy alloys. *Mater. Trans.* **44**, 2020–2024 (2003).
59. Sun, Q. et al. Magnetic domains and domain wall pinning in atomically thin $CrBr_3$ revealed by nanoscale imaging. *Nat. Commun.* **12**, 1989 (2021).
60. Yang, B., Motz, C., Rester, M. & Dehm, G. Yield stress influenced by the ratio of wire diameter to grain size – a competition between the effects of specimen microstructure and dimension in micro-sized polycrystalline copper wires. *Philos. Mag.* **92**, 3243–3256 (2012).
61. Chen, J., Chen, Y., Liu, J., Liu, T. & Dai, L. Anomalous size effect in micron-scale CoCrNi medium-entropy alloy wire. *Scr. Mater.* **199**, 113897 (2021).
62. Su, J., Raabe, D. & Li, Z. Hierarchical microstructure design to tune the mechanical behavior of an interstitial TRIP-TWIP high-entropy alloy. *Acta Mater.* **163**, 40–54 (2019).
63. Ming, K., Lu, W., Li, Z., Bi, X. & Wang, J. Amorphous bands induced by low temperature tension in a non-equiatomic CrMnFeCoNi alloy. *Acta Mater.* **188**, 354–365 (2020).
64. Xue, Q. & Cerreta, E. Gray G. Microstructural characteristics of post-shear localization in cold-rolled 316L stainless steel. *Acta Mater.* **55**, 691–704 (2007).
65. Zhao, S. et al. Amorphization in extreme deformation of the CrMnFeCoNi high-entropy alloy. *Sci. Adv.* **7**, eabb3108 (2021).
66. Han, S., Zhao, L., Jiang, Q. & Lian, J. Deformation-induced localized solid-state amorphization in nanocrystalline nickel. *Sci. Rep.* **2**, 493 (2012).
67. Subhash, G., Awasthi, A., Kunka, C., Jannotti, P. & DeVries, M. In search of amorphization-resistant boron carbide. *Scr. Mater.* **123**, 158–162 (2016).
68. Gratz, A., Deloach, L., Clough, T. & Nellis, W. Shock amorphization of cristobalite. *Science* **259**, 663–666 (1993).
69. Ovid'ko, I. Nanoscale amorphization as a special deformation mode in nanowires. *Scr. Mater.* **66**, 402–405 (2012).
70. Wang, H. et al. Deformation-induced crystalline-to-amorphous phase transformation in a CrMnFeCoNi high-entropy alloy. *Sci. Adv.* **7**, eabe3105 (2021).
71. Wu, W., Ni, S., Liu, Y., Liu, B. & Song, M. Amorphization at twin-twin intersected region in FeCoCrNi high-entropy alloy subjected to high-pressure torsion. *Mater. Charact.* **127**, 111–115 (2017).
72. Jiang, K. et al. Abnormal hardening and amorphization in an FCC high entropy alloy under extreme uniaxial tension. *Int. J. Plast.* **159**, 103463 (2022).
73. Bu, Y. et al. Elastic strain-induced amorphization in high-entropy alloys. *Nat. Commun.* **15**, 4599 (2024).
74. Hagiwara, M., Inoue, A. & Masumoto, T. Mechanical-properties of Fe-Si-B amorphous wires produced by in-rotating-water spinning method. *Metal. Trans. Phys. Metall. Mater. Sci.* **13**, 373–382 (1982).
75. Avettand, M., Marinova, M., Taillard, R. & Jiang, W. Thermal stability, phase transformations and mechanical properties of a $Fe_{64}B_{24}Y_4Nb_6$ metallic glass. *J. Alloy. Compd.* **854**, 157068 (2021).

Acknowledgements

The authors thank Dr. Chaochao Dun and Dr. Penghua Ge for the fruitful discussion, Dr. Hui Li for the help with the APT experiment, and the anonymous reviewers for their contribution to the peer review of this work. This work is supported by the National Natural Science Foundation of China (Grant No. 52171165 and 52301158), Ningbo Key Research and Development Program (Grant No. 2023Z097), and the Major Fundamental Research Program of Hunan Province in China (Grant No. 2024JC0003).

Author contributions

W.M. Yang, J.W. Li, Y.Q. Dong, Q.K. Man, H.S. Liu, Z.M. Li, and A. Inoue designed the research. Yan Ma and Z.D Kou performed all the tests. W.M. Yang, J.W. Li, and Z.M. Li analyzed the data. Yan Ma, Z.D. Kou, A.N. He, W.M. Yang, and J.W. Li wrote the manuscript with contributions from the other authors. All authors commented on the final manuscript and conclusions of this work.

Competing interests

The authors declare no competing interests.

Additional information

Supplementary information The online version contains supplementary material available at https://doi.org/10.1038/s41467-024-54984-7.

Correspondence and requests for materials should be addressed to Weiming Yang or Jiawei Li.

Peer review information *Nature Communications* thanks Pawel Czaja, Suhash Dey, and the other, anonymous, reviewer(s) for their contribution to the peer review of this work. A peer review file is available.